Electrocatalytic Study for Hydrogen Evolution Reaction on MoS_2/BP and MoSSe/BP in Acidic Media

Arunima Singh*, Preeti Bhumla, Manjari Jain, Saswata Bhattacharya*

Department of Physics, Indian Institute of Technology Delhi, Hauz Khas, New Delhi:110016, India

E-mail: saswata@physics.iitd.ac.in[SB],Arunima.Singh@physics.iitd.ac.in[AS]

Phone: +91-2659 1359. Fax: +91-2658 2037

Abstract

Molecular hydrogen (H_2) production by electrochemical hydrogen evolution reaction (HER) is being actively explored for non-precious-metal based electrocatalysts that are earth-abundant and low cost like MoS_2. Although it is acid-stable, its applicability is limited by catalytically inactive basal plane, poor electrical transport and inefficient charge transfer at the interface. Therefore, the present work examines its bilayer van der Waals heterostructure (vdW HTS). The second constituent monolayer Boron Phosphide (BP) is advantageous as an electrode material owing to its chemical stability in both oxygen and water environments. Here, we have performed first-principles based calculations under the framework of density functional theory (DFT) for HER in an electrochemical double layer model with the BP monolayer, MoS_2/BP and MoSSe/BP vdW HTSs. The climbing image nudged elastic band method (CI-NEB) has been employed to determine the minimum energy pathways for Tafel and Heyrovsky reactions. The calculations yield that Tafel reaction shows no reaction barrier. Thereafter, for

Heyrovsky reaction, we have obtained low reaction barrier in the vdW HTSs as compared to that in the BP monolayer. Subsequently, we have observed no significant difference in the reaction profile of MoS_2/BP and MoSSe/BP vdW HTSs in case of high coverage (25%) and 1/3 H^+ concentration (conc.). However, in the case of small coverage (11%) and 1/3 H^+ conc., MoSSe/BP shows feasible Heyrovsky reaction with no reaction barrier. Finally, on comparing the coverages with 1/4 H^+ conc., we deduce high coverage with low conc. and low coverage with high conc. to be apt for HER via Heyrovsky reaction path.

Introduction

The availability of clean and renewable energy source governs the tenable development. Innovation in systems like fuel cells, metal-air batteries and water electrolysis positively impacts the environment.[1] The cleanest alternative for the same is the molecular hydrogen (H_2) and hence, in the present context, we consider materials that support its production.[2,3] The electrochemical reactions that are in sync with the clean environment aim involve hydrogen oxidation reaction (HOR), oxygen reduction reaction (ORR), hydrogen evolution reaction (HER) and oxygen evolution reaction (OER).[4] The former two are associated with fuel cells, while the latter two are associated with water splitting or water electrolysis. There exists wide range of materials that can catalyze these electrochemical reactions by photocatalytic or electrocatalytic pathways.[5–7] The present paper focuses on HER by the electrocatalysts. HER requires large overpotential to be initiated, and therefore catalysts are required to lower the overpotential.[8] In this respect, Pt has established itself to be an efficient catalyst.[9] However, its high cost and low abundance have urged the scientific community to find new materials for catalytic applications.[10] In fact, any heterogeneous catalysis under periodic boundary conditions faces the challenge of possessing an apt catalytic material that decreases the reaction barrier.[11]

HER can occur in both acidic and alkaline media. In either of the media, the reaction steps

follow (i) adsorption of H, (ii) its reduction and (iii) desorption as H_2.[12] Now, HER has been reported to have sluggish kinetics in alkaline media with ambiguous active sites.[13] Since the electrolytic reactions at the electrode are acidic, we are focusing on the acidic media in the present study. The adsorption step is very fast and is termed as the Volmer step:[14]

Volmer reaction (fast): $H^+ + e^- \rightarrow H_{ad}$

The subsequent steps take place either as Tafel or Heyrovsky paths.

Tafel reaction: $2H_{ad} \rightarrow H_2$

Heyrovsky reaction: $H_{ad} + H^+ + e^- \rightarrow H_2$

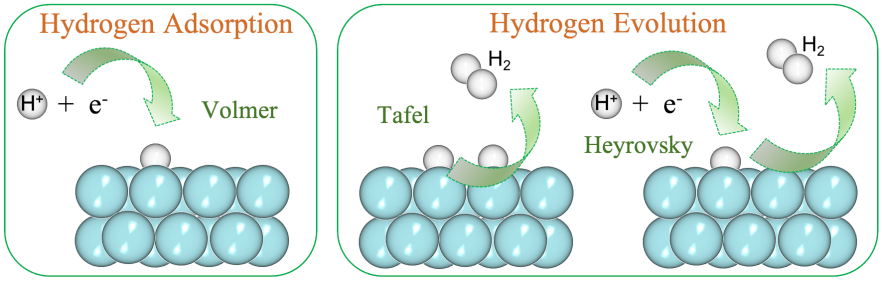

Figure 1: (Color online) HER Steps: Volmer is the adsorption step, and Tafel/Heyrovsky is the evolution step.

As previously mentioned, the concept is to obtain material for the reaction that does not include precious metals like Pt. The literature has shown the transition metals (Fe, Ni, Co), carbides, metal oxides (RuO_2, IrO_2), graphene, non-layered 2D materials, metal–organic frameworks (MOFs) and transition metal dichalcogenides (TMDs) as effective HER catalysts.[8,12,15–19] We restrict our study to the 2D materials that showcase quantum confinement effects with increased carrier mobility and large surface area.[20,21] This results in their increased catalytically active sites. The monolayer TMDs (in place of graphene) have established themselves as a potent material with optimal band gap suitable for optoelectronics, photocatalysis and electrocatalysis.[22–27] In addition, due to their flexibility, these are widely studied for flexible electronic devices. Literature has reported their use as catalysts for HER, especially on the surface of 1T′-MoS_2 and edge sites of 2H-MoS_2.[28,29] MoS_2 being acid-stable is an added advantage.[30] Furthermore, its heterojunctions have also shown promising HER

catalytic behaviour.[13,31–33] It is pertinent to mention here that the tunability of 2D materials for specific applications is prevalent by defect engineering, strain engineering, stacking order, external field implementation, alloying and forming heterojunctions.[34–38] Amongst them, formation of heterojunctions with van der Waals forces in between the constituent monolayers are classified under van der Waals heterostructures (vdW HTSs). These have proved a real boon to the field of work because the constituent monolayers retain their properties simultaneously with their combined vdW HTS properties. In addition, the electronegativity difference between the constituent monolayers actuates electron transfer, thereby affecting the HER.[39] Even if the constituent monolayers have inactive sites, the resulting vdW HTS can be obtained as an active electrocatalyst due to an inbuilt electric field at the interface.[40] Presently, we explore Boron Phosphide (BP) monolayer, MoS_2/BP and MoSSe/BP vdW HTSs for HER. Recent works have reported vdW HTSs with BP instead of graphene as it has a similar single atomic layered hexagonal structure, however, along with a band gap.[41] BP monolayer has been reported with low carrier effective mass, high carrier mobility, good mechanical strength, and stability in water environments.[42,43] Since the lattice parameter of MoS_2 and BP is similar, the MoS_2/BP vdW HTS becomes a plausible system with minimal lattice mismatch.[44] BP monolayer has also been synthesized experimentally .[45] In addition, since Janus (MoSSe) has established itself with more catalytically active sites than MoS_2, we have also analyzed MoSSe/BP vdW HTS. Any prior investigations for HER on these systems are hitherto unknown; hence we have considered these systems for our work.

The aforementioned HER reaction path should be accounted for the proton and electron free energies. These are incorporated by the computational hydrogen electrode model as proposed by Norskov *et al.*[14] The model caters to the fundamental problem of large-scale calculation of a real system along with electrolyte by following the electrochemical double layer approach rather than external charge formation. The underlying approximation considers solvated proton upto first bilayer. Until now, no study has been reported with the analysis of vdW HTSs by computational hydrogen electrode model for HER in acidic media to the best of our

knowledge.[46] We have initially discussed the stacking configuration and electronic structure. Subsequently, the computational hydrogen electrode model is discussed. Thereafter, Tafel and Heyrovsky reaction paths are analyzed. Finally, we discuss the electrode potential, and the reaction and activation energies.

Methodology

The first-principles based density functional theory (DFT) calculations have been employed in the present work.[47–52] The associated code chosen is Vienna *ab initio* simulation package (VASP)[53–55] with projector augmented wave (PAW) pseudopotentials using plane wave basis. The generalized gradient approximation (GGA) that accounts for the exchange-correlation (xc) interaction amongst electrons is incorporated by PBE xc functional (as proposed by Perdew-Burke-Ernzerhof (PBE)[56,57]). The Brillouin zone (BZ) sampling of 2×2 K-mesh is used for conjugate gradient minimization with an energy tolerance of 0.001 meV and the force tolerance of 0.001 eV/Å. The intermediate, initial and final energetics are obtained by the BZ sampling of 6×6 K-mesh. The plane wave cut-off energy is set to 500 eV. All the structures are built with 20 Å vacuum that avoids the electrostatic interactions among the periodic images. The two-body Tkatchenko-Scheffler vdW scheme has been employed for obtaining optimized structures.[58,59] This is an iterative scheme based on Hirshfeld partitioning of the electron density. We have employed climbing-image nudged elastic band (CI-NEB) method to obtain minimum energy path for HER.[60,61] Note that we have not explicitly considered entropic calculations, as in approximation of solvated proton on first layer, 0.2 - 0.3 eV can be added all along the energetics.[14] In reference to the previous literature, we have not included the spin-orbit coupling (SOC) in our calculations.[62–64]

Results and Discussions

Heterostructure

The present paper features BP monolayer, MoS_2/BP and MoSSe/BP vdW HTSs for HER assessment. The lattice parameter of BP monolayer is 3.20 Å and that of MoS_2 is 3.16 Å. Since the lattice mismatch between them is less (1.2% as obtained by (l(MoS_2) - l(BP))/l(BP), where l(MoS_2) and l(BP) is the lattice constant of MoS_2 and BP, respectively), the corresponding MoS_2/BP vdW HTS formed is commensurate.[65] Its corresponding structural and electronic properties are obtained by unit cell configuration (see Fig. S1-S3 in Supplementary Information (SI)), whereby, MoS_2/BP and MoSSe/BP form type 1 and type 2 alignment and it corroborates with the prior research.[44,66] Note that, initially, two stacking styles (see Fig. 2 (a) and (b)) between the constituent monolayers were considered, wherein the stacking corresponding to Fig. 2 (b) has minimum binding energy.[31] Therefore, we have proceeded with this stacking in our work.

HER Study

Now, we advance on HER study, for which we have constituted 2×2 and 3×3 supercells. The former being smaller restricts the proton concentration (conc.) variability, therefore we need larger supercells. In view of this, we are analyzing 2×2 supercell along with 3×3, because unlike monolayer, the vdW HTS with further large supercell size becomes computationally demanding. The subsequent paragraphs discuss the concepts of coverage and proton conc. for clarity.

The first step is to obtain the coverage that gives $\Delta G_H \simeq 0$ for our study. The number of adsorbed hydrogen (H_{ads}) per surface atoms is defined as the coverage. ΔG_H is the free energy of atomic hydrogen adsorption and is expressed as:

$$\Delta G_H = \Delta E_H + \Delta E_{ZPE} - T\Delta S_H$$

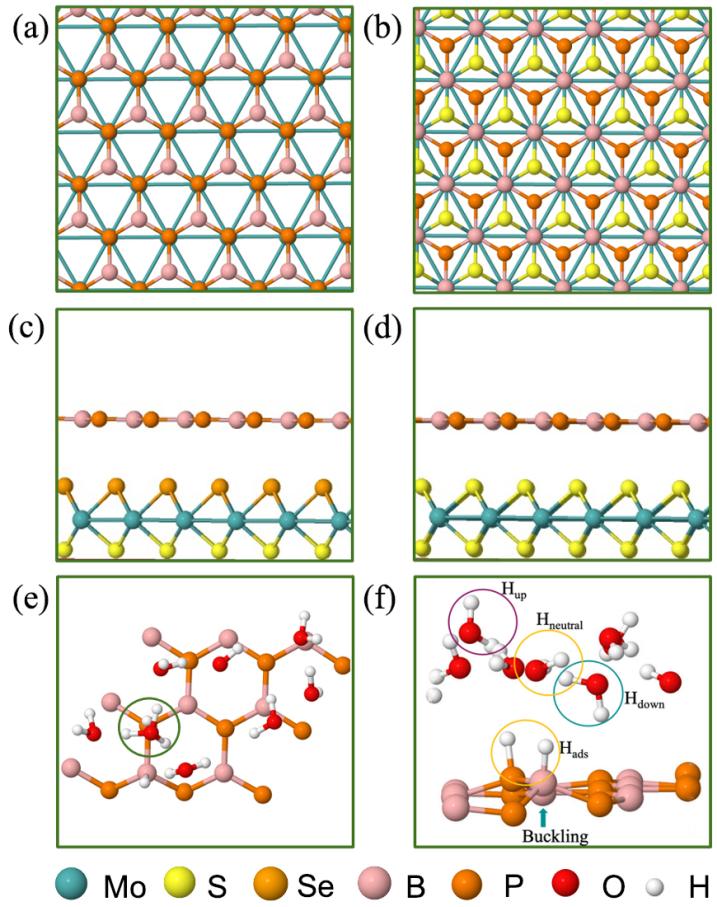

Figure 2: (Color online) (a) and (b) Top view of MoS_2/BP vdW HTS stacking configurations, (c) and (d) Side view of minimum energy stacking configuration for MoSSe/BP and MoS_2/BP vdW HTSs, respectively, (e) 3×3 supercell of BP monolayer schematic with 1/3 H^+ conc. i.e., 1 $H^+/3H_2O$, (f) Water molecule orientations of H_{up}, H_{down} and $H_{neutral}$. Buckling on BP can be observed at the H_{ads} site.

where,

$$\Delta E_H = E[nH] - E[(n\text{-}1)H] - 1/2E[H_2]$$

In the aforementioned equations, ΔE_H is the hydrogen binding energy on the surface of vdW HTS, E[nH] (or E[(n-1)H]) is the energy of the configuration with n (or n-1) number of H_{ads}, ΔE_{ZPE} is the zero-point energy of H_{ads} and ΔS_H is the entropy of H_2 in the gas phase. At 298 K, $\Delta E_{ZPE} - T\Delta S_H = 0.25$ eV is well established in literature.[30] We observe 2×2 supercell with 25% H coverage ($2H_{ads}$ per 8 surface atoms) and 3×3 supercell with 11% H coverage ($2H_{ads}$ per 18 surface atoms) with ΔG_H equal to -0.024 eV and 0.049 eV, respectively. We

have deduced these coverages after trials upto 38%. We have chosen consecutive B and P atomic sites for H_{ads} as this configuration was found to be the most stable. Also, we observed buckling at the site of H_{ads} (see Fig. 2 (f)).

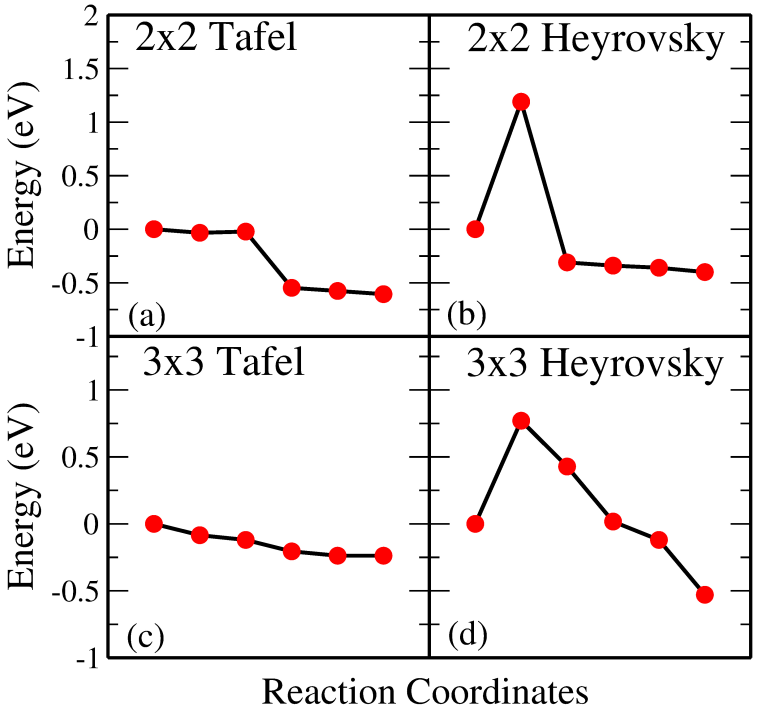

Figure 3: (Color online) 2×2 supercell of BP monolayer showing (a) Tafel reaction path and (b) Heyrovsky reaction path. 3×3 supercell of BP monolayer showing (c) Tafel reaction path and (d) Heyrovsky reaction path.

We now discuss the optimized systems consisting of water layer (water-solid interface with 3 Å thick water layer) without and with solvated protons (i.e., H^+). Fig. 2 (e) shows the BP monolayer ($2H_{ads}$) with H^+ in 3×3 supercell. Note that the H^+ is in the form of hydronium (H_3O) in the water layer. 2×2 supercell is a small supercell and therefore, only 1 H^+ is been considered. However, the corresponding H_2O molecules in the water layer are varied, thereby constituting 1/3 (i.e., 1 $H^+/3H_2O$) and 1/4 (i.e., 1 $H^+/4H_2O$) H^+ conc. The configuration corresponding to 3×3 supercell size has been studied for 1/8 (i.e., 1 $H^+/8H_2O$) H^+ conc. The water orientation (see Fig. 2 (f)) over the H_{ads} species is flat and H_{up} orientation is usually seen on the topmost layer. Further, all H_2O molecules are not H_{down}, rather, they are at some angular orientations other than strict H_{up} and H_{down} configurations. These orientations

are essential because the electrostatic potential, as seen from the solid surface, also depends on the same. The stability of the vdW HTS along with water layer orientation is established by the similar profile of radial distribution plot at 0K and 300K (see Fig. S6 in SI).

Tafel Reaction Step

Fig. 3(a) and 3(b) give Tafel and Heyrovsky reaction steps, respectively on the BP monolayer. This corresponds to the 2×2 supercell with 3 H_2O molecules and 1/3 H^+ conc., respectively.

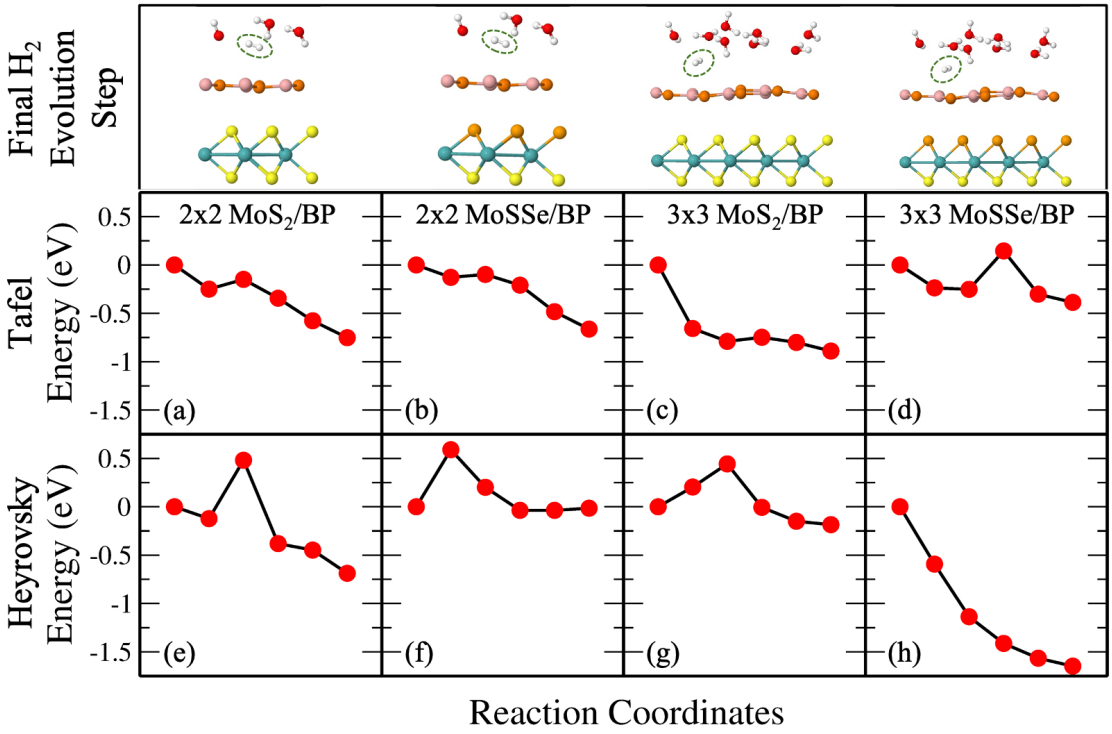

Figure 4: (Color online) (a)-(d) Tafel reaction path (upper row) on MoS_2/BP and MoSSe/BP vdW HTSs for 2×2 supercell and 3×3 supercell. (e)-(f) Heyrovsky reaction path (lower row) on MoS_2/BP and MoSSe/BP vdW HTSs for 2×2 supercell and 3×3 supercell.

The BP monolayer acts as a reference to analyze the reactions for the MoS_2/BP and MoSSe/BP vdW HTSs. Here, we observe a reaction barrier in Heyrovsky reaction step (1.19 eV) and not in case of the Tafel reaction step. The reaction steps for 3×3 supercell and 1/8 H^+ conc. are given in Fig. 3(c) and 3(d), whereby the Tafel reaction steps show no

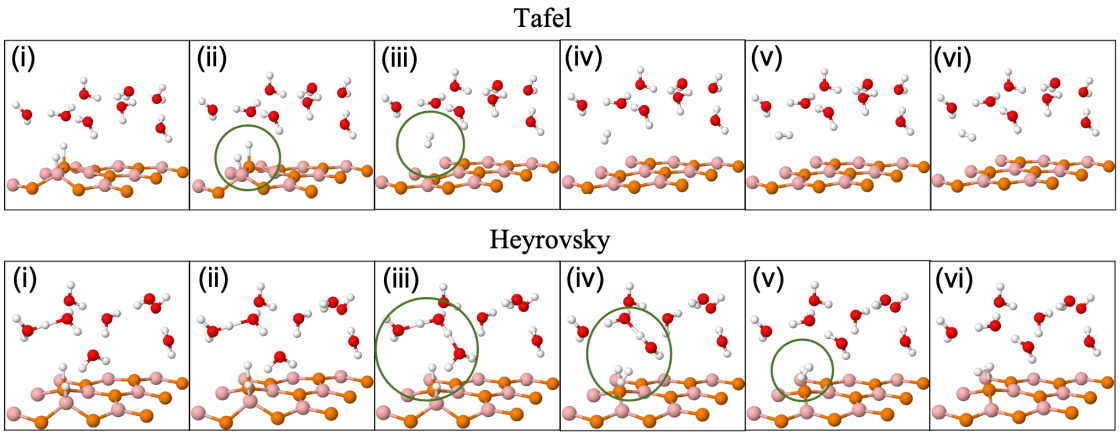

Figure 5: (Color online) Tafel (upper row) and Heyrovsky (lower row) reaction profile snapshots on 3×3 BP surface.

barrier and Heyrovsky reaction steps show reduced reaction barrier as compared to that in 2×2 supercell. Further, we first discuss the Tafel reaction step analysis for the vdW HTSs. Fig. 4 highlights the Tafel reaction step on the MoS_2/BP ((a) and (c)) and MoSSe/BP ((b) and (d)) vdW HTSs. Firstly, no significant difference is observed between MoS_2/BP and MoSSe/BP vdW HTSs for 2×2 supercell. However, we observe reaction barrier only in case of MoSSe/BP 3×3 supercell (0.14 eV). The overview of the Tafel reaction analysis is consistent with Tafel being surface reaction, thereby, less or no observed reaction barrier. We observed that the minimum energy profile in Tafel reaction is not continuously decreasing; instead, a slight hump is present. This corresponds to the buckling in the BP monolayer. As previously mentioned, the site of H_{ads} is buckled with respect to other sites, and during the H_2 evolution process, the corresponding BP site adjusts itself to the planar configuration (see Fig. 5). Note that BP surface is considered for the reaction analysis as basal plane of MoS_2 is not catalytically active.

Heyrovsky Reaction Step

Unlike Tafel, the Heyrovsky reaction step is not a pure surface reaction. It involves charge transfer, thereby affecting the reaction barrier and Fig. 4 (e)-(h) substantiates the same. We have observed reduction in reaction barrier in the vdW HTSs as compared to that

in BP monolayer (refer Fig. 3 and Fig. 4). The 3×3 supercell configuration puts forth decreased reaction barrier than in the case of 2×2 supercell configuration. The MoS_2/BP and MoSSe/BP demonstrates this reduction from 0.48 eV (Fig. 4 (e)) to 0.43 eV (Fig. 4 (g)) and 0.59 eV (Fig. 4 (f)) to 0 eV (Fig. 4 (h)), respectively. The reduced coverage and hence reduced charge redistribution on the surface can be attributed to the reduced reaction barrier in the 3×3 supercell. Further, we observe significant change in case of MoSSe and this may be attributed to the combined effect of the coverage and the electronegativity difference within the MoSSe layer that affects the charge transfer at the interface.

Apart from the factors that are discussed above, there are structural parameters that affect the reaction steps. The bonds of H in H_3O stretch before combining with the H_{ads}. At the transition state, H_2 is formed. After that, the atoms adjust themselves to low energy configuration. After the intermediate step, the B and P atoms adjust, corresponding to H_{ads}, along with the other H_2O molecules. As in the Tafel scenario, the steps post H_2 formation optimize the H_2 molecule in the water layer. The reaction barrier, therefore, depends on the buckling in the monolayer, the water molecule's orientation, and the coexisting water molecules with H^+ (see Fig. 5).

Finally, we discuss the Heyrovsky reaction in MoS_2/BP for 1/4 H^+ conc. both in case of 2×2 (i.e., 1 $H^+/4H_2O$) and 3×3 (i.e., 2 $H^+/8H_2O$) supercells. We observed reaction barrier decreases from 0.48 eV (Fig. 4 (e)) to 0.09 eV (Fig. 6 (a)) and 0.59 eV (Fig. 4 (g)) to 0 eV (Fig. 6 (b)) in 2×2 and 3×3 supercells, respectively. This indicates that high coverage prefers low H^+ conc. and vice versa for reduction in reaction barrier. We correlate this with the overpotential of the reaction, as discussed in the following section. Overpotential is the difference between the experimentally obtained reaction potential and the electrode potential. The electrode potential is analyzed only in the Heyrovsky reaction as it involves proton transfer. Therefore, this affects the work function and the potential at which the reaction takes place.

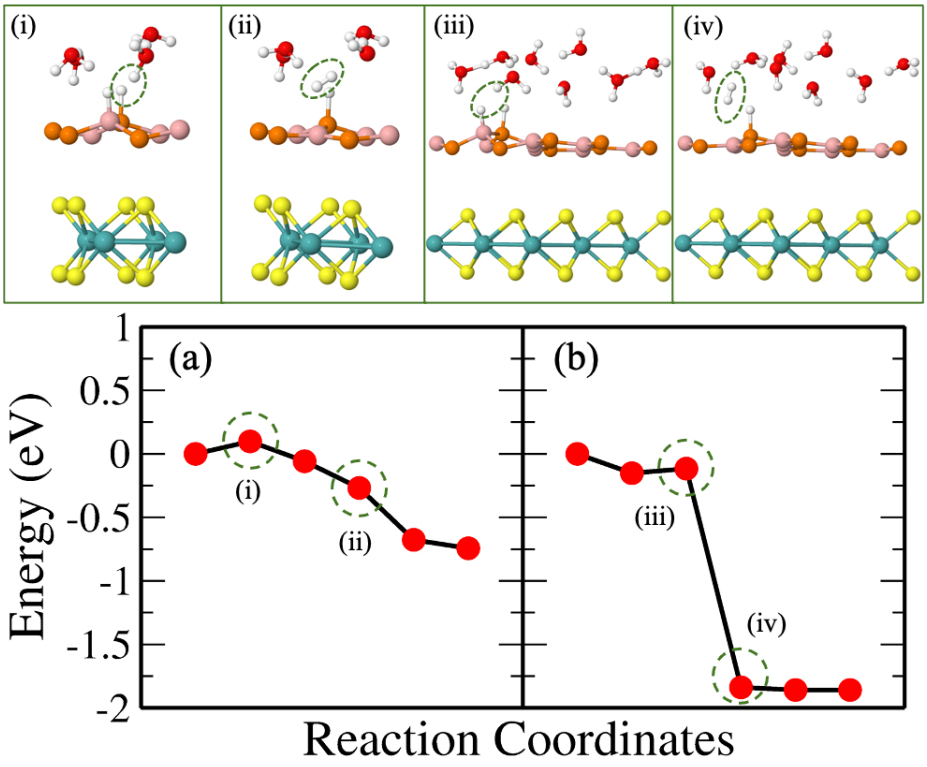

Figure 6: (Color online) Heyrovsky reaction path for MoS_2/BP vdW HTS with 1/4 H^+ conc. in (a) 2×2 supercell and (b) 3×3 supercell.

Electrode Potential

Table 1: Electrode potential (U) of MoS_2/BP and MoSSe/BP with and without H^+ in water layer.

vdW HTSs	With H^+		Without H^+	
	U_1 (V)	U_2 (V)	U_1 (V)	U_2 (V)
MoS_2/BP (2×2)	-2.31	0.48	1.04	0.70
MoSSe/BP (2×2)	-1.83	1.07	-0.68	1.31
MoS_2/BP (3×3)	-2.09	-0.05	-0.09	0.84
MoSSe/BP (3×3)	-2.55	0.90	-0.79	1.19

The electrode potential (U) of the slab is reported relative to the normal hydrogen electrode (NHE):

$$U = \phi - \phi_{NHE}$$

Here ϕ (E_{vac} - E_{fermi}) is the work function, and ϕ_{NHE} is taken to be 4.44 eV.[14,30,67] The work

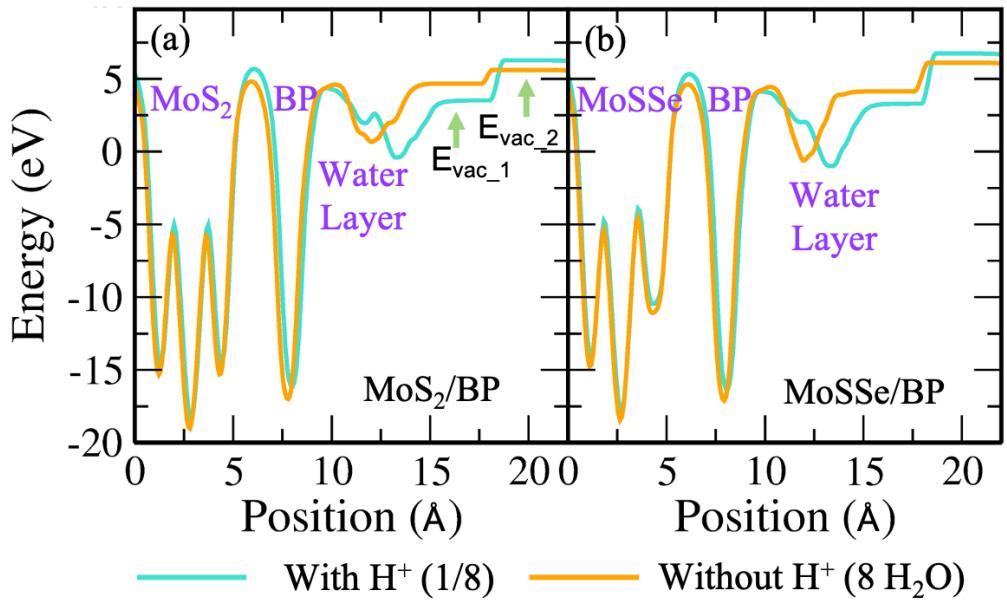

Figure 7: (Color online) Electrostatic potential plot of MoS_2/BP and MoSSe/BP vdW HTSs depicting water layer with and without H^+. (a) and (b) 3×3 supercell with 1/8 H^+ conc. and 8 H_2O molecules.

function depends on the surface H coverage, the thickness or number of water bilayers, the water molecule orientation, and the system size. In small systems (here 2×2), the range of electrode potential analysis is limited to a few H^+ conc. considerations. Fig. 7 presents the electrostatic potential plot where we have deduced the work function of 3×3 MoS_2/BP and MoSSe/BP. The same for 2×2 MoS_2/BP and MoSSe/BP is shown in Fig. S9 of SI. The potential drops are evident in Fig. 7, with a significant drop at the interface of BP and the water layer. The values of U corresponding to water layer with and without H^+ are reported in Table 1, which are in the range of -2.5 V to 1.3 V. We have incorporated dipole corrections as the vdW HTSs with two different surfaces maintain two potentials. Moreover, the H_{ads} and, therefore, the coverage affects the dipole-dipole interactions. As a result, we report the two values of U, i.e., U_1 and U_2, corresponding to two vacuum levels of E_{vac_1} and E_{vac_2}, respectively.

As previously discussed the dependence of ϕ on water orientation, we have explicitly optimized the H_{down} configuration for H_2O molecules. The Heyrovsky reaction path for the same

in MoS_2/BP and MoSSe/BP 3×3 supercells can be seen in Fig. S10 (a) and (b) of SI. The obtained barrier is reduced as compared to the 2×2 supercells of MoS_2/BP, MoSSe/BP and 3×3 supercell of MoS_2/BP. The corresponding electrode potential is also reported in Fig. S10 (c) and (d).

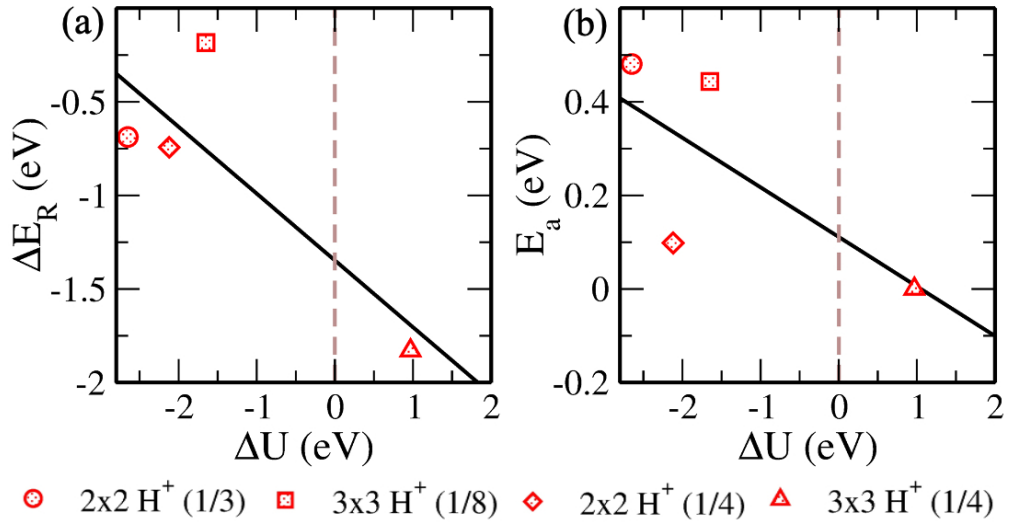

Figure 8: (Color online) Variation of (a) reaction energy ($\Delta E_R = E_{final} - E_{initial}$) and (b) activation energy (E_a), of configurations with respect to the change in electrode potential ($\Delta U = U_{1_{initial}} - U_{1_{final}}$) from initial to final.

Now we progress towards the extrapolation approach to cater the problem of potential change from initial to final in case of proton transfer Heyrovsky reaction. In this approach, we obtain reaction energies and activation energies of system with different supercell sizes and H^+ conc. The former represents the energy difference between initial and final states, while the latter is the amount of energy required to overcome the reaction barrier. Thereafter we obtain ΔE_R and E_a vs ΔU plot. The ΔU signifies change in electrode potential from initial to final. Moreover, the change in U_1 (corresponding to water layer potential) is significant as compared to the change in U_2 (corresponding to MoS_2 layer potential). The potential drop and charge transfer would accordingly affect the U_1 and U_2. Hence, the reaction taking place at BP layer surface is crucial and we must consider U_1 for our analysis of electrode potential. Therefore, the ΔU represented in the plot is corresponding to the U_1. On extrapolating the ΔE_R to $\Delta U = 0$, we obtain -1.33 eV. The negative value indicates the spontaneity of

the Heyrovsky reaction step. In case of positive ΔE_R, the Heyrovsky reaction would have been the rate determining step. The corresponding E_a is obtained at 0.11 eV. Hence, on comparing vdW HTS with monolayer, the synergistic effect of the two layers play role in affecting the overpotential and hence the reaction mechanism.

Conclusion

In summary, we have modelled a dynamically stable MoS_2/BP and MoSSe/BP vdW HTSs. They have been studied for HER by computational hydrogen electrode model. The optimized structure with the water layer showed a significant potential drop at the surface-water interface. The electrostatic potential is further affected by the proton solvated in water layer and the H_{ads} constituting coverage over the surface. 2×2 supercell with 25% H coverage and 3×3 supercell with 11% H coverage have been deduced for the calculations. Firstly, the MoS_2/BP and MoSSe/BP vdW HTSs show reduced barrier height for both Tafel and Heyrovsky reactions in comparison to the BP monolayer. Tafel reaction, being a surface reaction does not require charge transfer, herein corroborates with no or less barrier observed in the MoS_2/BP and MoSSe/BP vdW HTSs. In case of Heyrovsky reaction, reduced reaction barrier has been reported. The reduced H^+ conc. in small supercell and 25% coverage substantiates the reduced barrier. Further, there is no significant difference between the MoSSe/BP and MoS_2/BP vdW HTS, as observed from the minimum energy reaction paths, except in the case of 11% coverage of MoSSe/BP with no reaction barrier. Hence, the MoSSe based vdW HTS has shown Heyrovsky reaction favoured HER for low coverage. On comparing the supercells (and hence different coverages) with respect to the same H^+ conc., we observe high coverage to favour low H^+ conc. and vice versa for reduced reaction barrier. Finally, as per the extrapolation approach for ΔE_R vs ΔU, the Heyrovsky reaction mechanism is established as favourable.

Supporting Information

(i) Structural, electronic and optical properties of MoS_2/BP and MoSSe/BP. (ii) Planar averaged charge density plot of MoS_2/BP and MoSSe/BP. (iii) Planar averaged charge density plot of MoS_2/BP with 1 solvated H^+. (iv) Radial distribution function at 0K and 300K temperatures for MoS_2/BP configuration. (v) 3×3 MoS_2/BP configurations. (vi) 3×3 MoS_2/BP configurations with H_{down} water layer orientation. (vii) Electrode potential of 2×2 MoS_2/BP and MoSSe/BP. (viii) H_{down} water orientation reaction path and electrode potential. (ix) Tafel reaction steps for 2×2 MoS_2/BP in case of $4H_2O$.

Acknowledgement

AS acknowledges IIT Delhi for the senior research fellowship. PB acknowledges UGC, India, for the senior research fellowship [1392/(CSIR- UGC NET JUNE 2018)]. MJ acknowledges CSIR, India, for the senior research fellowship [grant no. 09/ 086(1344)/2018-EMR-I]. SB acknowledges the financial support SERB under his Core Research Grant [CRG/2019/000647]. We acknowledge the High Performance Computing (HPC) and Veena Cluster facility at IIT Delhi for computational resources.

References

(1) Zhang, X.; Chen, A.; Chen, L.; Zhou, Z. 2D materials bridging experiments and computations for electro/photocatalysis. *Advanced Energy Materials* **2022**, *12*, 2003841.

(2) Chu, S.; Majumdar, A. Opportunities and challenges for a sustainable energy future. *Nature* **2012**, *488*, 294–303.

(3) Seh, Z. W.; Kibsgaard, J.; Dickens, C. F.; Chorkendorff, I.; Nørskov, J. K.;

Jaramillo, T. F. Combining theory and experiment in electrocatalysis: Insights into materials design. *Science* **2017**, *355*, 4998.

(4) Vij, V.; Sultan, S.; Harzandi, A. M.; Meena, A.; Tiwari, J. N.; Lee, W.-G.; Yoon, T.; Kim, K. S. Nickel-based electrocatalysts for energy-related applications: oxygen reduction, oxygen evolution, and hydrogen evolution reactions. *ACS Catalysis* **2017**, *7*, 7196–7225.

(5) Lu, Q.; Yu, Y.; Ma, Q.; Chen, B.; Zhang, H. 2D transition-metal-dichalcogenide-nanosheet-based composites for photocatalytic and electrocatalytic hydrogen evolution reactions. *Advanced Materials* **2016**, *28*, 1917–1933.

(6) Cao, L.; Wang, C. Metal–Organic Layers for Electrocatalysis and Photocatalysis. *ACS Central Science* **2020**, *6*, 2149–2158.

(7) Jin, H.; Song, T.; Paik, U.; Qiao, S.-Z. Metastable two-dimensional materials for electrocatalytic energy conversions. *Accounts of Materials Research* **2021**, *2*, 559–573.

(8) Zhang, H.; Yang, X.; Zhang, H.; Ma, J.; Huang, Z.; Li, J.; Wang, Y. Transition-Metal Carbides as Hydrogen Evolution Reduction Electrocatalysts: Synthetic Methods and Optimization Strategies. *Chemistry–A European Journal* **2021**, *27*, 5074–5090.

(9) Hansen, J. N.; Prats, H.; Toudahl, K. K.; Mørch Secher, N.; Chan, K.; Kibsgaard, J.; Chorkendorff, I. Is there anything better than Pt for HER? *ACS Energy Letters* **2021**, *6*, 1175–1180.

(10) Zhao, G.; Chen, J.; Sun, W.; Pan, H. Non-Platinum Group Metal Electrocatalysts toward Efficient Hydrogen Oxidation Reaction. *Advanced Functional Materials* **2021**, *31*, 2010633.

(11) Shi, Y.; Ma, Z.-R.; Xiao, Y.-Y.; Yin, Y.-C.; Huang, W.-M.; Huang, Z.-C.; Zheng, Y.-Z.; Mu, F.-Y.; Huang, R.; Shi, G.-Y., et al. Electronic metal–support interaction modulates

single-atom platinum catalysis for hydrogen evolution reaction. *Nature Communications* **2021**, *12*, 1–11.

(12) Jin, H.; Guo, C.; Liu, X.; Liu, J.; Vasileff, A.; Jiao, Y.; Zheng, Y.; Qiao, S.-Z. Emerging two-dimensional nanomaterials for electrocatalysis. *Chemical Reviews* **2018**, *118*, 6337–6408.

(13) Wei, J.; Zhou, M.; Long, A.; Xue, Y.; Liao, H.; Wei, C.; Xu, Z. J. Heterostructured electrocatalysts for hydrogen evolution reaction under alkaline conditions. *Nano-Micro Letters* **2018**, *10*, 1–15.

(14) Skúlason, E.; Karlberg, G. S.; Rossmeisl, J.; Bligaard, T.; Greeley, J.; Jónsson, H.; Nørskov, J. K. Density functional theory calculations for the hydrogen evolution reaction in an electrochemical double layer on the Pt (111) electrode. *Physical Chemistry Chemical Physics* **2007**, *9*, 3241–3250.

(15) Wang, Y.; Zhang, Z.; Mao, Y.; Wang, X. Two-dimensional nonlayered materials for electrocatalysis. *Energy & Environmental Science* **2020**, *13*, 3993–4016.

(16) Wang, Y.; Zhang, H.; Yang, X.; Ma, J.; Huang, Z.; Li, J. Recent advances in transition-metal carbides: from controlled preparation to hydrogen evolution reaction application. *Chemistry (Weinheim an der Bergstrasse, Germany)* **2020**, *118*, 5074–5090.

(17) Du, J.; Li, F.; Sun, L. Metal–organic frameworks and their derivatives as electrocatalysts for the oxygen evolution reaction. *Chemical Society Reviews* **2021**, *50*, 2663–2695.

(18) Esposito, D. V.; Hunt, S. T.; Kimmel, Y. C.; Chen, J. G. A new class of electrocatalysts for hydrogen production from water electrolysis: metal monolayers supported on low-cost transition metal carbides. *Journal of the American Chemical Society* **2012**, *134*, 3025–3033.

(19) Trasatti, S. Physical electrochemistry of ceramic oxides. *Electrochimica Acta* **1991**, *36*, 225–241.

(20) Mir, S. H.; Yadav, V. K.; Singh, J. K. Recent advances in the carrier mobility of two-dimensional materials: a theoretical perspective. *ACS Omega* **2020**, *5*, 14203–14211.

(21) Zhang, X.; Wang, B.; Niu, X.; Li, Y.; Chen, Y.; Wang, J. Bi2OS2: a direct-gap two-dimensional semiconductor with high carrier mobility and surface electron states. *Mater. Horiz.* **2018**, *5*, 1058–1064.

(22) Singh, A.; Basera, P.; Saini, S.; Kumar, M.; Bhattacharya, S. Importance of Many-Body Dispersion in the Stability of Vacancies and Antisites in Free-Standing Monolayer of MoS_2 from First-Principles Approaches. *The Journal of Physical Chemistry C* **2020**, *124*, 1390–1397.

(23) Chen, Y.; Huang, S.; Ji, X.; Adepalli, K.; Yin, K.; Ling, X.; Wang, X.; Xue, J.; Dresselhaus, M.; Kong, J., et al. Tuning electronic structure of single layer MoS_2 through defect and interface engineering. *ACS Nano* **2018**, *12*, 2569–2579.

(24) Rao, C.; Gopalakrishnan, K.; Maitra, U. Comparative study of potential applications of graphene, MoS_2 , and other two-dimensional materials in energy devices, sensors, and related areas. *ACS Applied Materials & Interfaces* **2015**, *7*, 7809–7832.

(25) Singh, E.; Singh, P.; Kim, K. S.; Yeom, G. Y.; Nalwa, H. S. Flexible molybdenum disulfide (MoS2) atomic layers for wearable electronics and optoelectronics. *ACS Applied Materials & Interfaces* **2019**, *11*, 11061–11105.

(26) Zeng, H.; Liu, G.-B.; Dai, J.; Yan, Y.; Zhu, B.; He, R.; Xie, L.; Xu, S.; Chen, X.; Yao, W., et al. Optical signature of symmetry variations and spin-valley coupling in atomically thin tungsten dichalcogenides. *Scientific Reports* **2013**, *3*, 1608.

(27) Wang, C.-Y.; Guo, G.-Y. Nonlinear optical properties of transition-metal dichalcogenide MX2 (M= Mo, W; X= S, Se) monolayers and trilayers from first-principles calculations. *The Journal of Physical Chemistry C* **2015**, *119*, 13268–13276.

(28) Wang, H.; Xiao, X.; Liu, S.; Chiang, C.-L.; Kuai, X.; Peng, C.-K.; Lin, Y.-C.; Meng, X.; Zhao, J.; Choi, J., et al. Structural and electronic optimization of MoS2 edges for hydrogen evolution. *Journal of the American Chemical Society* **2019**, *141*, 18578–18584.

(29) Chen, J.; Li, F.; Tang, Y.; Tang, Q. Tuning the phase stability and surface HER activity of 1T$^{/}$-MoS_2 by covalent chemical functionalization. *Journal of Materials Chemistry C* **2020**, *8*, 15852–15859.

(30) Tang, Q.; Jiang, D.-e. Mechanism of hydrogen evolution reaction on 1T-MoS2 from first principles. *ACS Catalysis* **2016**, *6*, 4953–4961.

(31) Singh, A.; Jain, M.; Bhattacharya, S. MoS_2 and Janus (MoSSe) based 2D van der Waals heterostructures: emerging direct Z-scheme photocatalysts. *Nanoscale Advances* **2021**, *3*, 2837–2845.

(32) Ling, F.; Kang, W.; Jing, H.; Zeng, W.; Chen, Y.; Liu, X.; Zhang, Y.; Qi, L.; Fang, L.; Zhou, M. Enhancing hydrogen evolution on the basal plane of transition metal dichacolgenide van der Waals heterostructures. *NPJ Computational Materials* **2019**, *5*, 20.

(33) Keivanimehr, F.; Habibzadeh, S.; Baghban, A.; Esmaeili, A.; Mohaddespour, A.; Mashhadzadeh, A. H.; Ganjali, M. R.; Saeb, M. R.; Fierro, V.; Celzard, A. Electrocatalytic hydrogen evolution on the noble metal-free MoS2/carbon nanotube heterostructure: a theoretical study. *Scientific Reports* **2021**, *11*, 1–9.

(34) Wan, J.; Lacey, S. D.; Dai, J.; Bao, W.; Fuhrer, M. S.; Hu, L. Tuning two-dimensional nanomaterials by intercalation: materials, properties and applications. *Chemical Society Reviews* **2016**, *45*, 6742–6765.

(35) Zhao, J.; Deng, Q.; Bachmatiuk, A.; Sandeep, G.; Popov, A.; Eckert, J.; Rümmeli, M. H. Free-standing single-atom-thick iron membranes suspended in graphene pores. *Science* **2014**, *343*, 1228–1232.

(36) Bao, W.; Jing, L.; Velasco, J.; Lee, Y.; Liu, G.; Tran, D.; Standley, B.; Aykol, M.; Cronin, S.; Smirnov, D., et al. Stacking-dependent band gap and quantum transport in trilayer graphene. *Nature Physics* **2011**, *7*, 948–952.

(37) Feng, J.; Qian, X.; Huang, C.-W.; Li, J. Strain-engineered artificial atom as a broad-spectrum solar energy funnel. *Nature Photonics* **2012**, *6*, 866–872.

(38) Wang, F.; Zhang, Y.; Tian, C.; Girit, C.; Zettl, A.; Crommie, M.; Shen, Y. R. Gate-variable optical transitions in graphene. *Science* **2008**, *320*, 206–209.

(39) Zhao, G.; Rui, K.; Dou, S. X.; Sun, W. Heterostructures for electrochemical hydrogen evolution reaction: a review. *Advanced Functional Materials* **2018**, *28*, 1803291.

(40) Bawari, S.; Kaley, N. M.; Pal, S.; Vineesh, T. V.; Ghosh, S.; Mondal, J.; Narayanan, T. N. On the hydrogen evolution reaction activity of graphene–hBN van der Waals heterostructures. *Physical Chemistry Chemical Physics* **2018**, *20*, 15007–15014.

(41) Şahin, H.; Cahangirov, S.; Topsakal, M.; Bekaroglu, E.; Akturk, E.; Senger, R. T.; Ciraci, S. Monolayer honeycomb structures of group-IV elements and III-V binary compounds: First-principles calculations. *Physical Review B* **2009**, *80*, 155453.

(42) Wu, J.; Li, J.-H.; Yu, Y.-X. Single Nb or W atom-embedded BP monolayers as highly selective and stable electrocatalysts for nitrogen fixation with low-onset potentials. *ACS Applied Materials & Interfaces* **2021**, *13*, 10026–10036.

(43) Vu, T. V.; Kartamyshev, A.; Hieu, N. V.; Dang, T. D.; Nguyen, S.-N.; Poklonski, N.; Nguyen, C. V.; Phuc, H. V.; Hieu, N. N. Structural, elastic, and electronic properties of

chemically functionalized boron phosphide monolayer. *RSC Advances* **2021**, *11*, 8552–8558.

(44) Mohanta, M. K.; Rawat, A.; Jena, N.; Dimple,; Ahammed, R.; De Sarkar, A. Interfacing boron monophosphide with molybdenum disulfide for an ultrahigh performance in thermoelectrics, two-dimensional excitonic solar cells, and nanopiezotronics. *ACS Applied Materials & Interfaces* **2019**, *12*, 3114–3126.

(45) Padavala, B.; Frye, C.; Wang, X.; Ding, Z.; Chen, R.; Dudley, M.; Raghothamachar, B.; Lu, P.; Flanders, B.; Edgar, J. Epitaxy of boron phosphide on aluminum nitride (0001)/sapphire substrate. *Crystal Growth & Design* **2016**, *16*, 981–987.

(46) Wiensch, J. D.; John, J.; Velazquez, J. M.; Torelli, D. A.; Pieterick, A. P.; McDowell, M. T.; Sun, K.; Zhao, X.; Brunschwig, B. S.; Lewis, N. S. Comparative study in acidic and alkaline media of the effects of pH and crystallinity on the hydrogen-evolution reaction on MoS2 and MoSe2. *ACS Energy Letters* **2017**, *2*, 2234–2238.

(47) Martin, R. M. *Electronic structure: basic theory and practical methods*; Cambridge University Press, 2004.

(48) Martin, R. M.; Reining, L.; Ceperley, D. M. *Interacting Electrons*; Cambridge University Press, 2016.

(49) Freysoldt, C.; Grabowski, B.; Hickel, T.; Neugebauer, J.; Kresse, G.; Janotti, A.; Van de Walle, C. G. First-principles calculations for point defects in solids. *Reviews of Modern Physics* **2014**, *86*, 253.

(50) Feng, L.-p.; Su, J.; Chen, S.; Liu, Z.-t. First-principles investigations on vacancy formation and electronic structures of monolayer MoS_2. *Materials Chemistry and Physics* **2014**, *148*, 5–9.

(51) Hohenberg, P.; Kohn, W. Inhomogeneous electron gas. *Physical Review* **1964**, *136*, B864.

(52) Kohn, W.; Sham, L. J. Self-consistent equations including exchange and correlation effects. *Physical Review* **1965**, *140*, A1133.

(53) Kresse, G.; Furthmüller, J. Efficient iterative schemes for ab initio total-energy calculations using a plane-wave basis set. *Physical Review B* **1996**, *54*, 11169.

(54) Blöchl, P. E. Projector augmented-wave method. *Physical Review B* **1994**, *50*, 17953.

(55) Blum, V.; Gehrke, R.; Hanke, F.; Havu, P.; Havu, V.; Ren, X.; Reuter, K.; Scheffler, M. Ab initio molecular simulations with numeric atom-centered orbitals. *Computer Physics Communications* **2009**, *180*, 2175–2196.

(56) Stampfl, C.; Van de Walle, C. Density-functional calculations for III-V nitrides using the local-density approximation and the generalized gradient approximation. *Physical Review B* **1999**, *59*, 5521.

(57) Perdew, J. P.; Burke, K.; Ernzerhof, M. Generalized gradient approximation made simple. *Physical Review Letters* **1996**, *77*, 3865.

(58) Tkatchenko, A.; Scheffler, M. Accurate molecular van der Waals interactions from ground-state electron density and free-atom reference data. *Physical Review Letters* **2009**, *102*, 073005.

(59) Tkatchenko, A.; DiStasio Jr, R. A.; Car, R.; Scheffler, M. Accurate and efficient method for many-body van der Waals interactions. *Physical Review Letters* **2012**, *108*, 236402.

(60) Henkelman, G.; Uberuaga, B. P.; Jónsson, H. A climbing image nudged elastic band method for finding saddle points and minimum energy paths. *The Journal of Chemical Physics* **2000**, *113*, 9901–9904.

(61) Henkelman, G.; Jónsson, H. Improved tangent estimate in the nudged elastic band method for finding minimum energy paths and saddle points. *The Journal of Chemical Physics* **2000**, *113*, 9978–9985.

(62) Fu, C.-F.; Luo, Q.; Li, X.; Yang, J. Two-dimensional van der Waals nanocomposites as Z-scheme type photocatalysts for hydrogen production from overall water splitting. *Journal of Materials Chemistry A* **2016**, *4*, 18892–18898.

(63) Weng, J.; Gao, S.-P. A honeycomb-like monolayer of HfO 2 and the calculation of static dielectric constant eliminating the effect of vacuum spacing. *Physical Chemistry Chemical Physics* **2018**, *20*, 26453–26462.

(64) Ren, K.; Tang, W.; Sun, M.; Cai, Y.; Cheng, Y.; Zhang, G. A direct Z-scheme PtS 2/arsenene van der Waals heterostructure with high photocatalytic water splitting efficiency. *Nanoscale* **2020**, *12*, 17281–17289.

(65) Rahman, A. U.; Morbec, J. M.; Rahman, G.; Kratzer, P. Commensurate versus incommensurate heterostructures of group-III monochalcogenides. *Physical Review Materials* **2018**, *2*, 094002.

(66) Ren, K.; Sun, M.; Luo, Y.; Wang, S.; Yu, J.; Tang, W. First-principle study of electronic and optical properties of two-dimensional materials-based heterostructures based on transition metal dichalcogenides and boron phosphide. *Applied Surface Science* **2019**, *476*, 70–75.

(67) He, Q.; Chen, X.; Chen, S.; Liu, L.; Zhou, F.; Li, X.-B.; Wang, G. Electrochemical hydrogen evolution at the interface of monolayer VS2 and water from first-principles calculations. *ACS Applied Materials & Interfaces* **2018**, *11*, 2944–2949.

Electrocatalytic Study for Hydrogen Evolution Reaction on MoS_2/BP and MoSSe/BP in Acidic Media†

Arunima Singh*, Preeti Bhumla, Manjari Jain, Saswata Bhattacharya*

Department of Physics, Indian Institute of Technology Delhi, New Delhi 110016, India

E-mail: saswata@physics.iitd.ac.in[SB],Arunima.Singh@physics.iitd.ac.in[AS]

Phone: +91-2659 1359. Fax: +91-2658 2037

Supporting Information

I. Structural, Electronic and Optical Properties of MoS_2/BP and MoSSe/BP

II. Planar Averaged Charge Density Plot of MoS_2/BP and MoSSe/BP

III. Planar Averaged Charge Density Plot of MoS_2/BP with 1 Solvated H^+

IV. Radial Distribution Function at 0K and 300K Temperatures for MoS_2/BP Configuration

V. 3×3 MoS_2/BP Configurations

VI. 3×3 MoS_2/BP Configurations with H_{down} Water Layer Orientation

VII. Electrode Potential of 2×2 MoS_2/BP and MoSSe/BP

Structural, Electronic and Optical Properties of MoS_2/BP and MoSSe/BP

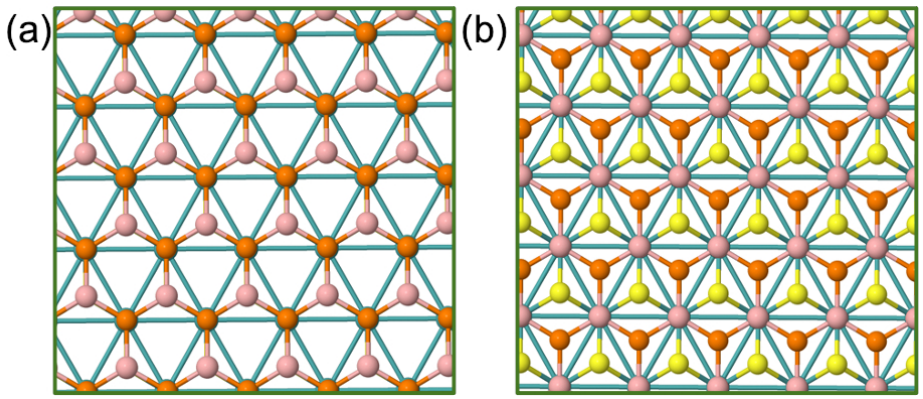

Fig. S1: (Color online) (a) and (b) are the two stacking styles of MoS_2/BP analyzed in our study. Configuration (b) has minimum binding energy.

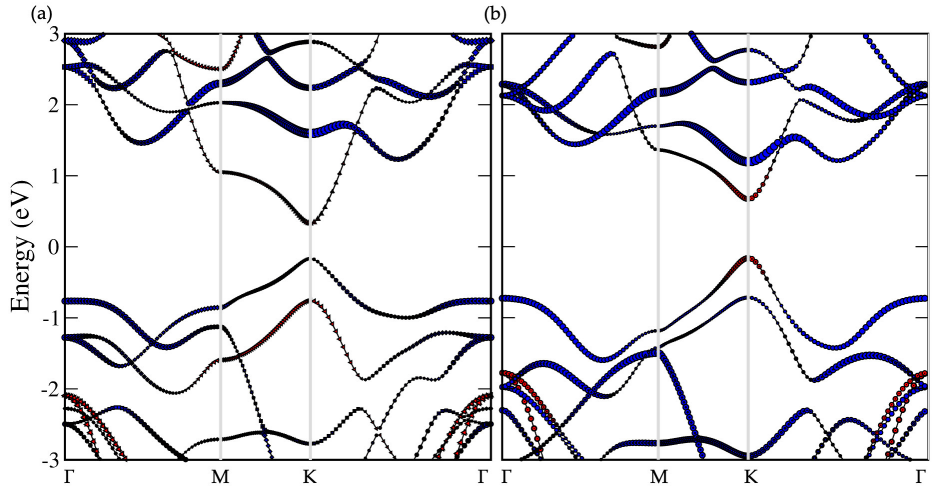

Fig. S2: (Color online) (a) Type II bandstructure obtained for MoSSe/BP vdW HTS; (b) Type I bandstructure obtained for MoS_2/BP vdW HTS. (xc functional: PBE)

In case of MoSSe/BP, BP contributes to the CBm (Conduction Band Minimum) and MoSSe contributes to the VBM (Valence Band Maximum). MoS_2/BP shows type 1 band edge alignment where MoS_2 straddles BP band edges.

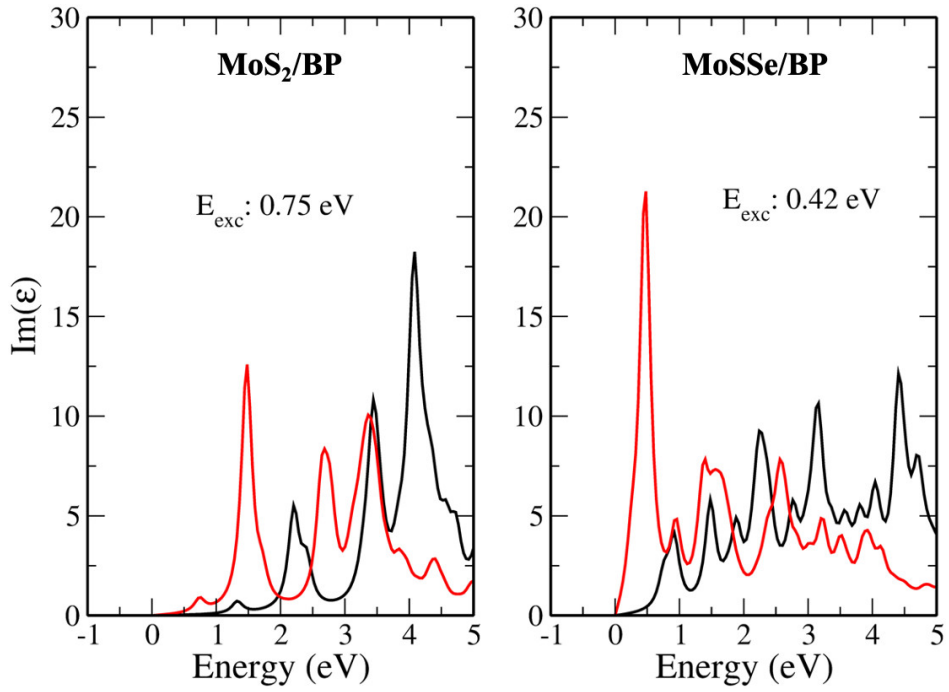

Fig. S3: (Color online) Exciton binding energy obtained for MoS_2/BP and MoSSe/BP vdW HTS.

The optical properties have also been calculated by the GW approach (Many Body Perturbation Theory (MBPT)). Fig. S3 shows the optical response using GW@BSE method that calculates the dielectric function. This is a complex function where the expression for interband process is the imaginary part thereby giving the absorption spectra. The real part (Re(ϵ)) is deduced from the Kramers-Kronig relation. We observe both the vdW HTSs (MoS_2/BP and MoSSe/BP) having response in the visible region. We have calculated the exciton binding energy (E_B) using the Bethe-Salpeter Equation. We observe small E_B that indicates its applicability in photoelectrochemical processes.

Planar Averaged Charge Density Plot of MoS_2/BP and MoSSe/BP

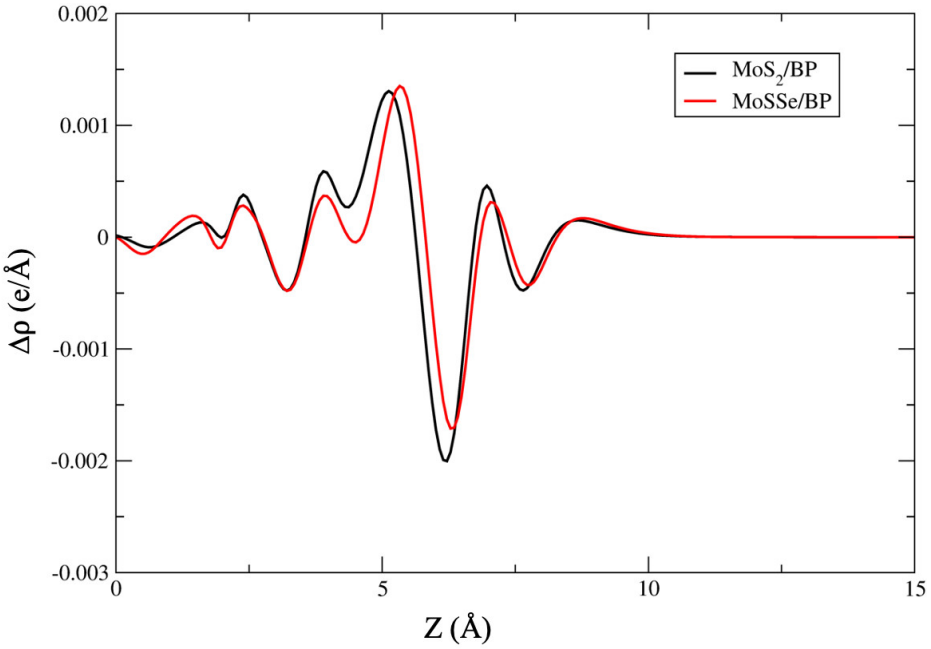

Fig. S4: (Color online) Planar averaged charge density plot for MoS_2/BP and MoSSe/BP vdW HTS.

The planar averaged charge density difference $\Delta\rho$ is calculated by:

$$\Delta\rho = \rho(\text{vdW HTSs}) - \rho(\text{MoS}_2 \text{ or MoSSe}) - \rho(\text{BP}) \tag{1}$$

where ρ(vdW HTSs), $\rho(MoS_2)$, ρ(MoSSe) and ρ(BP) are the charge densities of the vdW HTS, monolayer MoS_2, monolayer MoSSe and monolayer BP, respectively.

Planar Averaged Charge Density Plot of MoS_2/BP with 1 Solvated H^+

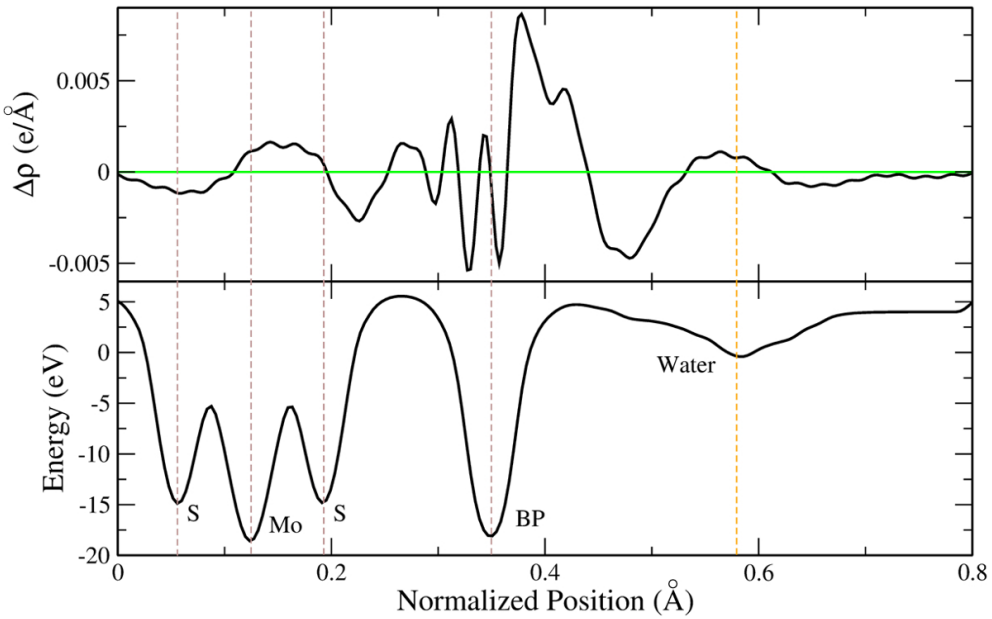

Fig. S5: (Color online) Planar averaged charge density and electrostatic potential plot for MoS_2/BP (with 1 H^+).

Fig. S5 shows the planar averaged charge density plot and the corresponding electrostatic potential plot for MoS_2/BP with 1 solvated H^+. The electrostatic potential plot explains the electrostatic potential corresponding to each atomic layer. We observe significant charge transfer at the BP and water interface.

Radial Distribution Function at 0K and 300K Temperatures for MoS_2/BP Configuration

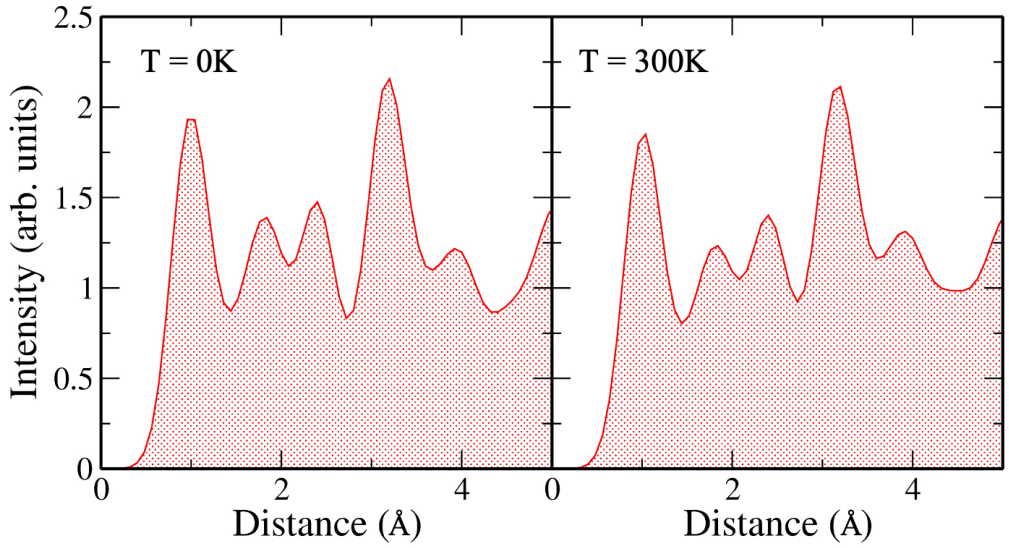

Fig. S6: (Color online) Radial distribution function of MoS_2/BP at two different temperatures T= 0K and T= 300K.

The radial distribution function here indicates the structural similarity of the MoS_2/BP with water layer at 0K and 300K. The water orientation thus obtained corroborates with the initial optimized configuration.

3×3 MoS_2/BP Configurations

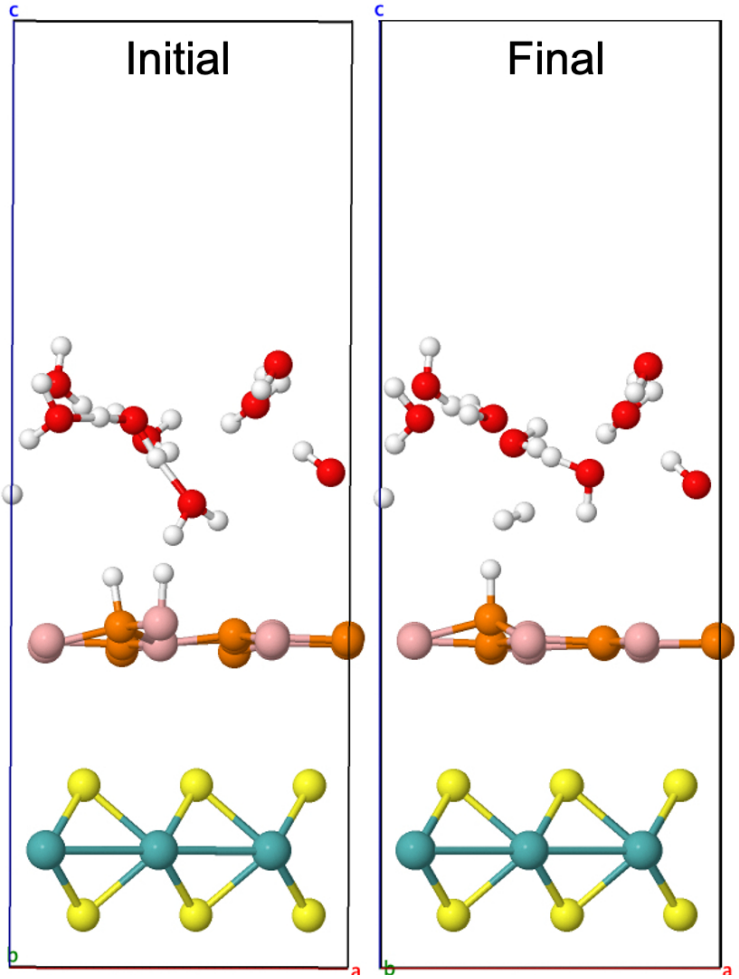

Fig. S7: (Color online) Initial and final configuration of 3×3 MoS_2/BP for Heyrovsky reaction.

3×3 MoS_2/BP Configurations With H_{down} Water Layer Orientation

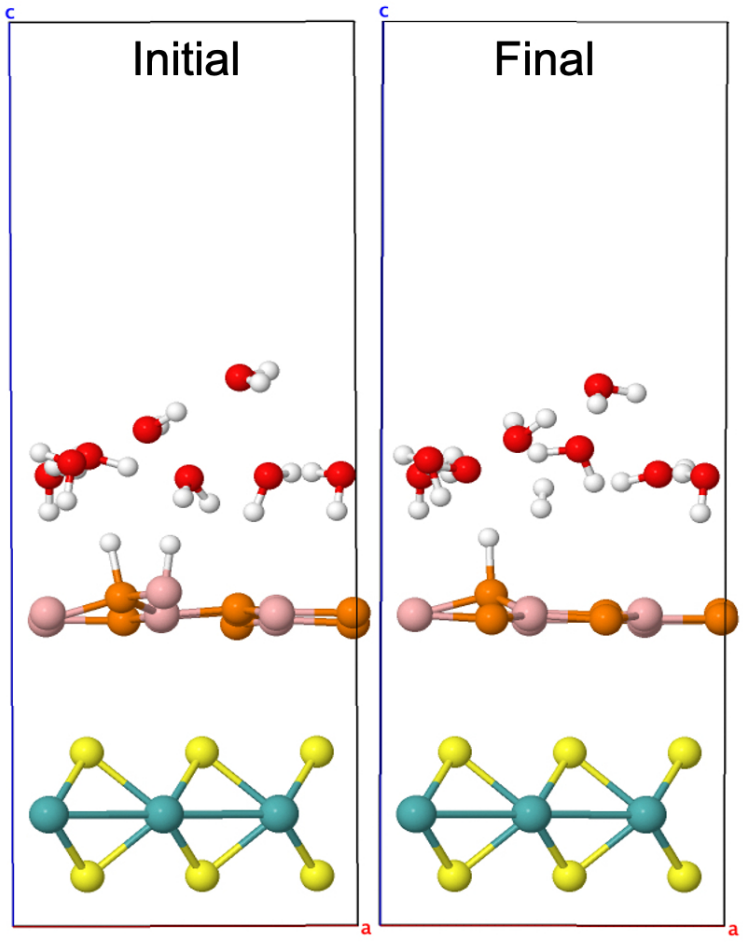

Fig. S8: (Color online) Initial and final configuration of 3×3 MoS_2/BP for Heyrovsky reaction in case H_{down} water layer orientation.

Electrode Potential of 2×2 MoS_2/BP and MoSSe/BP

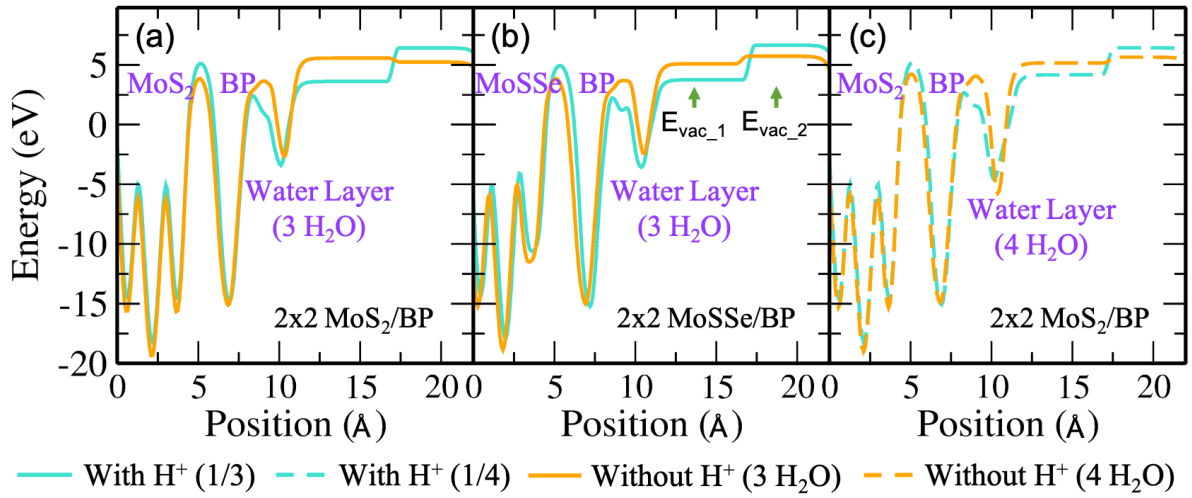

Fig. S9: (Color online) (a) Electrode potential for 2×2 MoS_2/BP with and without H^+ corresponding to 1/3 proton concentration and 3 H_2O, respectively. (b) Electrode potential for 2×2 MoSSe/BP with and without H^+ corresponding to 1/3 proton concentration and 3 H_2O, respectively. (c) Electrode potential for 2×2 MoS_2/BP with and without H^+ corresponding to 1/4 proton concentration and 4 H_2O, respectively.

H_{down} Water Orientation Reaction Path and Electrode Potential

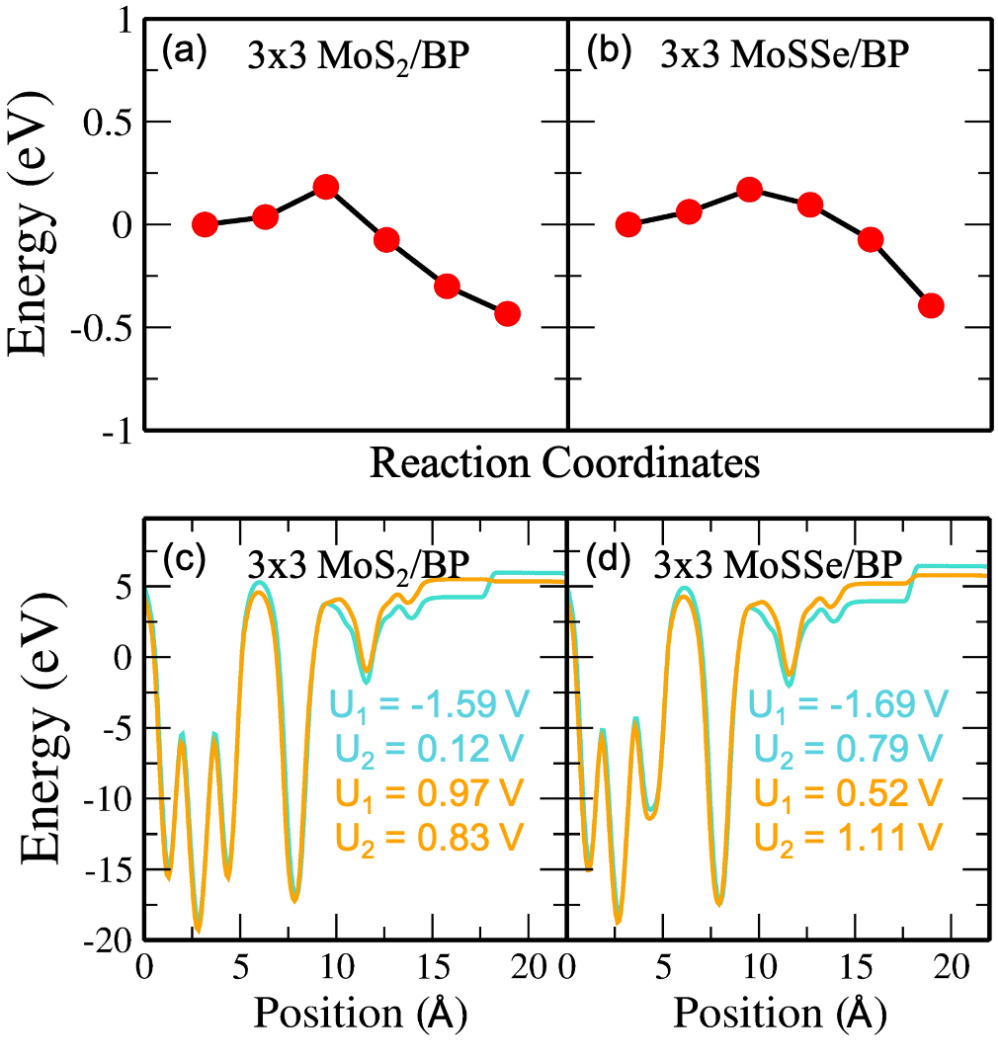

Fig. S10: (Color online) (a) and (b) Heyrovsky reaction step for MoS_2/BP and MoSSe/BP vdW HTS in 3×3 supercell with 1/8 proton concentration (c) and (d) Electrostatic potential plot of MoS_2/BP and MoSSe/BP vdW HTSs depicting water layer with and without H^+ in 3×3 supercell with 1/8 proton concentration and 8 water molecules, respectively.

Tafel Reaction Steps for 2×2 MoS_2/BP in case of $4H_2O$

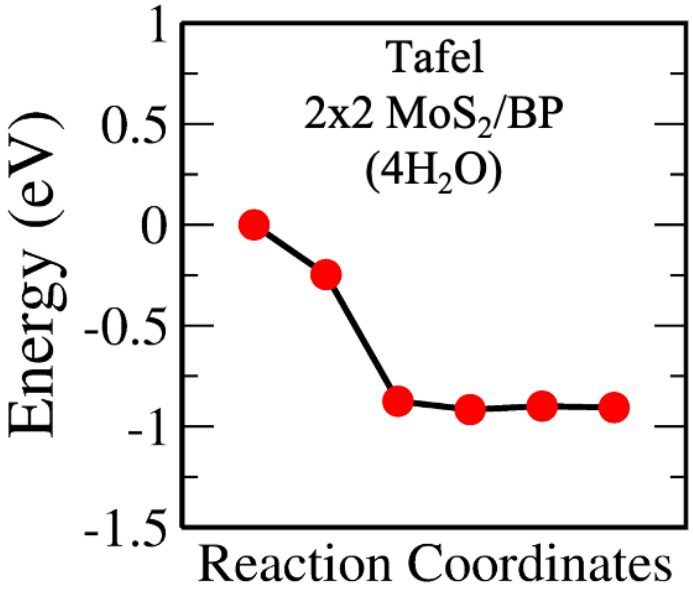

Fig. S11: (Color online) Tafel reaction step for 2×2 MoS_2/BP for 4 H_2O.